Role of Micro-tearing Mode in DIII-D and Future High-β_p Core Plasmas

X. Jian[1*], C.Holland[1], J.Candy[2], S. Ding[3,4], E. Belli[2], V.Chan[2], G.M.Staebler[2], A.M.Garofalo[2], J. Mcclenaghan[2] , P. Snyder[2]

1 University of California San Diego, 9500 Gilman Dr., La Jolla, California 92093-0417, USA
2 General Atomics, P.O. Box 85608, San Diego, California 92186-5608, USA
3 Oak Ridge Associated Universities, Oak Ridge, TN 37831, USA
4 Institute of Plasma Physics, Chinese Academy of Sciences, P.O. Box 1126, Hefei, Anhui, 230031, China
Author to whom correspondence should be addressed： xijian@ucsd.edu

Abstract: Excellent confinement has been routinely observed in DIII-D (J.L.Luxon, Nucl. Fusion, 2002) high β_p discharges, which are characterized by a strong large-radius internal transport barrier (ITB) in almost all kinetic channels. Typically, the ion thermal transport is neoclassical with conventional long-wavelength turbulence instabilities suppressed by α stabilization, while the mechanism for the anomalous electron thermal transport remains unclear (A.M.Garofalo, Nucl. Fusion, 2015). A new gyrokinetic analysis shows that while the large values of α in the ITB can stabilize all local electrostatic drift wave (ES-DW) instabilities as well as the kinetic ballooning mode, a new slab-like micro-tearing mode (MTM) with its eigenfunction mainly peaking on the high field slide is destabilized. This destabilization is shown to be more likely to happen in discharges with high safety factors. Nonlinear gyrokinetic simulations demonstrate that this MTM branch can reproduce the experimentally inferred electron thermal flux in the ITB region, and therefore provide convincing evidence that the electron temperature profile in the ITB is regulated by the MTM. Extrapolations to the future scenarios, like ITER high β_p plasmas, show that the dominant instability is likely to come back to ES-DW due to the lower density gradient and collisionality. However, even in this regime, some unusual features associated with MTMs predicted for DIII-D parameters, such as the high-field-side peaking and slab nature, may remain for the reactor ES-DW.

Key Words: High β_p, Microtearing modes, Transport

1. Introduction

Developing economically attractive steady-state tokamak reactor scenarios requires the simultaneous achievement of high plasma confinement (normally denoted by $H_{98,y2}$ with $H_{98,y2} = \tau_E / \tau_{E,th}^{IPB98(y,2)}$) and a high bootstrap current fraction ($f_{BS} = I_{BS} / I_p$, where I_{BS} and I_p the bootstrap current and total plasma current, respectively), in order to generate the desired amount of fusion power without requiring a significant fraction of that power to recirculate into external current drive actuators[1]. The high β_p scenario[2] (where $\beta_p = 2\mu_0 p / B_p^2$, and p and B_p are the plasma pressure and poloidal magnetic field, respectively), which is based on an advanced scenario pioneered in JT-60U[3, 4], can achieve high values of $H_{98,y2}$ through the formation of a strong large radius internal transport barrier (ITB). Since $f_{BS} \sim \beta_p$, the high β_p scenario is

intrinsically operated at a high bootstrap current fraction. Motivated by its compatibility with both high fusion gain and steady-state operation, heavy efforts are invested in devices such as DIII-D for the development of this scenario[5-9].

A key component of the high β_p scenario is the use of α stabilization[9-11], which is an inherent stabilization effect coming from the toroidal geometry of tokamaks, to achieve high confinement time and pressure. Specifically, $\alpha = -q^2(\partial_r V / 2\pi^2)(V / 2\pi^2 R_0)^{1/2}[4\pi\partial_r P / (rB_{unit}^2)^2]$ and is proportional to $-q^2 / B_{unit}^2 R_0 dp / dr$ in the limit of infinite aspect ratio shifted-circle geometry, where V, R_0 and B_{unit} is the flux surface volume, plasma major radius, and effective magnetic field strength, respectively. Large values of α can sufficiently modify the effective magnetic drift frequency to stabilize both microscopic and macroscopic instabilities. Here, r is the minor radius of the magnetic surface at the outboard midplane. Through this mechanism, potentially attractive operating scenarios with self-sustaining high confinement and self-generated bootstrap current (also proportional to dp / dr) can be developed.

In order to fully develop these scenarios and confidently extend them to future reactor parameters, it is essential to have a comprehensive understanding of the underlying transport physics, particularly of the crucial ITB region. Recent work has shown[5, 12] that in the ITB region of DIII-D high β_p discharges, the conventional drift-wave turbulence is suppressed via α stabilization. Transport modeling of these discharges using the TGYRO[13] solver indicates that the ion thermal transport is neoclassical across almost the entire plasma volume, while the electron transport remains anomalous. These studies utilized the NEO[14, 15] and TGLF[16, 17] models for neoclassical and turbulent transport predictions, respectively. However, questions remain regarding transport in these plasmas, namely identifying what instability or related physics mechanism drives the electron thermal transport, which is far larger than the neoclassical predictions[5, 12]. Without an understanding of the mechanism driving electron thermal transport, extrapolation of this scenario to future burning plasma machines[18, 19] faces large uncertainties. Specifically, extrapolation of present high-β_p scenarios to a future device such as ITER[1] with high confidence requires answering the following three questions:

1. Is the physics mechanism regulating the electron transport clear?
2. Can the physics be reproduced quantitatively by present reduced models?
3. How will the physics mechanism change between present and future machines?

In order to answer these questions, this paper is organized as follows. The background information of a representative DIII-D high-β_p shot, as well as the corresponding TGYRO transport modeling results will be briefly introduced in Section II. In Section III, a dedicated gyrokinetic analysis will reveal that the governing physics mechanism of electron energy transport in the ITB region is a novel micro-tearing mode (MTM) instability. This analysis is then used in

Section IV to interpret temperature profile predictions made via TGYRO transport modeling. In Section V, we carry out a corresponding gyrokinetic analysis of a representative ITER high β_p scenario that was developed through TGYRO predictive modeling. Finally, a summary of the results and discussion are given in Section VI. We note that the discharge detailed in Section II, and a subset of the results discussed in Section III, were first introduced in a previous letter by the authors in Ref. [20]. In this paper, we provide both greater details and an extended discussion of those results and highlight their implications when extrapolating from DIII-D to ITER-like parameters.

2. Experiments and TGYRO modeling

Global parameters and profiles for a typical DIII-D high-β_p discharge (shot number 176125) are shown in Figure 1. Time traces of global parameters are shown in Figure 1 (a)-(d). As can be seen, both β_N and β_p as well as $H_{98,y2} = \tau_E / \tau_{E,th}^{IPB98(y,2)}$ (here $\tau_E = W_{th} / (P_{th} - dW/dt)$, the stored thermal energy $W_{th} = W - W_f$ with W the total stored energy from the equilibrium reconstruction and W_f the stored energy contributed by fast ions inferred from an empirical formula fitted to ONETWO calculations. $P_{th} = P_{ohm} + P_{aux} - P_{floss}$, where P_{ohm} , P_{aux} and P_{floss} is the ohmic heating power, auxiliary injected power, and estimated NBI power loss by prompt charge exchange and unconfined orbits.) can be kept nearly stationary for hundreds of milliseconds, significantly longer than the energy confinement time of 100 ms, and suggesting the possibility of sustained stable operation desirable in a future steady-state reactor[19, 21]. For the rest of this paper, parameters and profiles drawn from a 20 ms averaging window centered at $t =$ 2.6 s (indicated by the dashed line in Fig 1(a)-(d)) are used. The profiles are shown in Figure 1(e)-(g) and average parameter values are given in Table I.

Fig. 1(e) shows that the toroidal current profile peaks off-axis due to the significant bootstrap current fraction, and consequently negative magnetic shear is created at a large radius (Fig 1(f)). The peaked off-axis bootstrap current comes from the large radius ITB of the pressure profile (Fig 1(g)). The synergistic interaction between the large radius ITB and negative shear enables both quantities to be self-consistently sustained in a stationary state. In this process, negative magnetic shear couples with the α -stabilization effect to suppress turbulence and transport locally[22], enabling the formation and sustainment of the ITB (and vice-versa). The profiles shown in Fig. 1(e)-(g) come from the OMFIT kineticEFIT module[23] which includes both motional Stark effect and kinetic profile measurements as constraints for the equilibrium reconstruction.

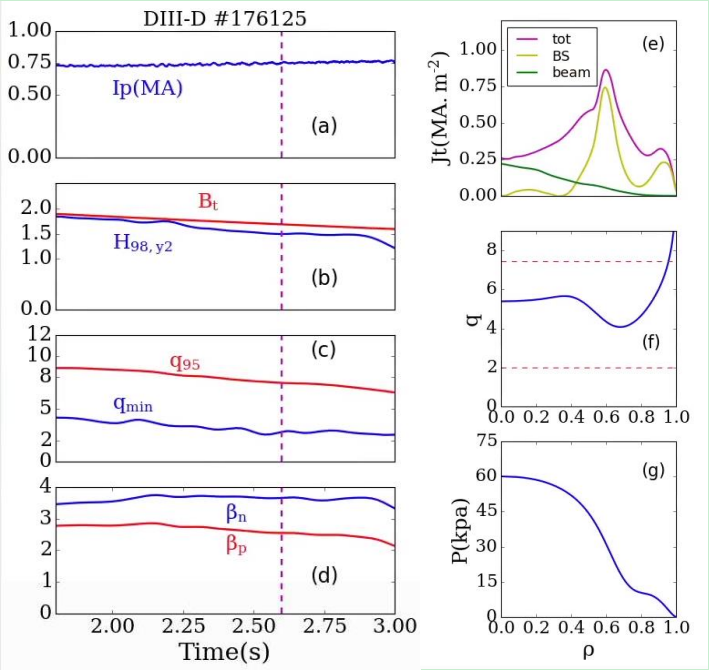

Figure 1. Time trace of I_p (a), B_t and $H_{98,y2}$ (b), q_{95} and $q_{\min}$ (c), β_N and β_p (d). The profiles of all the current components (e), q (f) and pressure (g) of t = 2.6s

Table I. Global parameters of 176125@2600ms

I_p (MA)	B_t (T)	β_N	β_p	q_{95}	$H_{98,y2}$
0.75	1.6	3.3	2.4	7.5	1.5

Figure 2 shows the results of TGYRO transport modeling, which predicts the kinetic profiles using prescribed sources (coming from the power balance analysis using the ONETWO[23] code) and transport models (TGLF and NEO) model for turbulent and neoclassical transport respectively. The radial region of ρ_{tor} = [0.4,0.8] is simulated to test whether the ITB region can be well reproduced by modeling. It is noted that the simulation data on axis is inferred from the gradient of ρ_{tor} = 0.4 and is plotted as well to give a better overall sense of the profile match between modeling and experimental profiles. As can be seen from Fig. 2(a) and (b), both T_i and T_e profiles are overestimated if both profiles are evolved simultaneously. Turbulent transport dominates the electron thermal flux Q_e (Fig. 2(c)) while the ion thermal flux Q_i (Fig. 2(d)) is

almost entirely neoclassical. The reason that T_i is overpredicted is that the predicted energy exchange between the ion and electron channels is too large due to the overprediction of T_e, as can be verified by only evolving T_i profile with T_e fixed to be the experimental profile. In the latter case, the T_i profile is shown to be well reproduced. We note that this phenomenon, namely that the neoclassical transport dominates for ion thermal transport while electron thermal transport cannot be well captured by TGLF, is actually widely observed in the modeling of DIII-D high-β_p plasmas, in particular, among the high q_{95} shots[5, 12]. Here, the TGLF SAT0[24] saturation model is used but switching to SAT1[25] does not significantly change the results. For this case, TGLF predicts TEM and ETG to be the dominant instabilities in the ITB region. In the next section the CGYRO[26] code, which is an advanced Eulerian gyrokinetic solver specifically designed and optimized for collisional and electromagnetic simulation, is used to understand the residual transport for Q_e in the ITB region and consequently the TGYRO result.

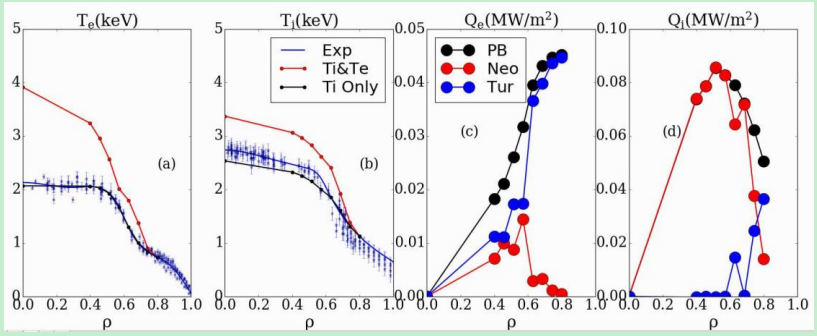

Figure 2. Comparison between experimental (blue line) and modeling profiles (of T_i (a) and T_e (b)) using TGYRO with T_i & T_e evolved simultaneously (red line) and T_i only evolved (black line). Comparison between the profiles of turbulent (denoted by 'Tur') and neoclassical ('Neo') transport flux of Q_e (c) and Q_i (d) for the case of T_i & T_e evolved simultaneously. 'PB' denotes the flux inferred from the ONETWO power balance analysis, with the collisional heat exchange self-consistently adjusted for the predicted profiles.

3. Gyrokinetic modeling results

For the more computationally expensive gyrokinetic analysis using CGYRO, we focus our analysis on a representative flux surface in the ITB region, ρ_{tor} = 0.6, where ρ_{tor} is the normalized toroidal flux. The background parameters are shown in Table II, where R and a are the plasma torus radius and minor radius of the whole plasma torus. $a/L_{T_e} = -a\nabla T_e / T_e$, $a/L_{T_i} = -a\nabla T_i / T_i$, $a/L_{n_e} = -a\nabla n_e / n_e$, $a/L_{n_C} = -a\nabla n_C / n_C$ (n_c is the carbon density),

$\nabla = d/dr$. s is the magnetic shear defined as $s = \frac{r}{q}\frac{dq}{dr}$, $\beta_{e,unit} = 8\pi n_e T_e / B_{unit}^2$ (See Ref[27] for the definition of B_{unit}), γ_E is the normalized shearing rate of E_r defined as $\gamma_E = -\frac{a}{c_s}\frac{r}{q}\frac{\partial \omega_0}{\partial r}$ where ω_0 is the toroidal rotation frequency induced by the E_r . ν_e is the collisionality defined as $\nu_e = \frac{a}{c_s}\frac{\sqrt{2}\pi e^4 n_e}{m_e^{1/2} T_e^{3/2}} \ln\Lambda$, where c_s , m_e and e is the ion sound speed, electron mass, and electron charge, respectively.

Table II. The experimental parameters of $\rho_{tor} = 0.6$

r/a	R/a	a/L_{Te}	a/L_{T_i}	a/L_{n_e}	a/L_{n_C}	n_C/n_e
0.62	3.05	4.1	2.7	3.4	5. 7	0.067
s	q	$\beta_{E,unit}$	α	$\gamma_E(c_s/a)$	$\nu_e(c_s/a)$	T_e/T_i
-0.80	4.3	5.9e-3	3.9	0.082	0.14	0.73

3.1 Linear analysis of the ITB region

To investigate the local gyrokinetic stability of the ITB region, we employ the CGYRO code. Unless otherwise noted, all simulations described in this paper use a 128-point velocity space grid (8 energies and 16 pitch angles), as well as 48 poloidal grid points with a 5th order differencing scheme in the parallel direction in configuration space. Three charged species (deuterium and carbon ions as well as electrons) are included, and magnetic shaping via a generalized Miller parameterization[28] is employed. Both the perpendicular and transverse magnetic perturbations are included. Collisions (like- and cross-species) are included via the Sugama model, which is a model for the complete linearized, gyroaveraged Fokker–Planck operator that is designed to conserve particles, momentum, and energy [29].

Previous studies show that α stabilization is efficient in electrostatic drift wave suppression for the high β_p scenario[5, 15, 20, 30]. Since $\alpha \sim q^2 (R/a)\beta_{e,unit} \sum_{j=e,i} (a/L_{T_j} + a/L_{n_j})$ [28, 31], our approach is to keep the ES-DW terms, like a/L_T and a/L_n (as well as β_e for electromagnetic simulation) fixed to experimental value but scale the α value, which can affect both the ES-DW [32] instabilities and kinetic ballooning mode (KBM)[33] via the geometric effect. Minor radius normalized scale lengths a/L_n and a/L_T are utilized in this paper because those are the relevant CGYRO internal variables, and R/a = 3.05 is held fixed throughout this study. We emphasize that although α scales with β_e, in this analysis α-stabilization is used to denote the purely geometrical effect (by scaling $\beta^* \sim dp/dr$ as defined in Eqs. 104, 109 and 112 of Ref[27]) which enters through the

magnetic drift terms in the gyrokinetic equation, and is separate from the self-consistent treatment of magnetic fluctuations and their coupling to electrostatic drift-waves. By a systematic scaling of α in the electrostatic limit, it is shown that all ES-DW, from long-wavelength trapped modes (TEMs) to short-wavelength electron temperature gradient (ETG) modes ($k_y\rho_s$ ranges from 0.1 to 50, where $k_y\rho_s$ of 50 corresponds to $k_y\lambda_{debye}$ ~1) are fully stabilized at α_{scale} =0.7 (Fig. 3(a)). Here α_{scale} is the scaling factor of the experimental α. Note that the ion temperature gradient (ITG) mode is found to be always stable in these conditions due to the low value of $\eta_i (= L_{ne} / L_{Ti})$, and so we do not expect that the electromagnetic (finite β) stabilization[30] of the ITG plays any role here. This interpretation is also consistent with the prediction of dominant neoclassical ion transport. More realistic electromagnetic calculations in which both perpendicular and transverse magnetic field fluctuations are retained show that the kinetic ballooning mode (KBM), instead of the TEM, is the dominant mode in the low-*k* region. However, similarly to the electrostatic modes, the KBM can be suppressed with an increase of α, and by α_{scale} = 0.7 the KBM is also fully suppressed. We note that the KBM discussed here is in the 'local (gyrokinetic)' sense while nonlocal effects that might destabilize the global KBM are not included. While all modes remain stable at the experimental value of α in the electrostatic case, in the electromagnetic case a new mode in the low-*k* region is destabilized as shown in Fig. 3(b). In order to clearly see how the dominant mode evolves with an increase of α, the frequency and growth rate for $k_y\rho_s$ = 0.2 as a function of α are shown in Fig. 3(c) and (d). The $k_y\rho_s$ = 0.2 KBM is fully suppressed by ~50% of the experimental α value, leaving a stable gap at larger α values. However, above 75% of the experimental α value, a new mode with phase velocity in the electron diamagnetic direction is destabilized by further increases in α. The mode is identified as a micro-tearing mode (MTM)[34, 35] based on the following analysis.

The eigenfunction of the electric potential ϕ and parallel magnetic potential $A_\parallel$ as a function of the ballooning angle θ are shown in Fig. 4(a) and (c), respectively, for this new mode. The clear tearing parity of the eigenmode structure is the first strong evidence supporting MTM identification. Interestingly, the eigenfunction has an extremely narrow peak at θ = 0 but is also highly extended in θ. Both the narrow peak and ballooning-space extension have been verified through poloidal resolution convergence tests. It is found that at least 48 points in poloidal grid points are required for converged results, nearly double the resolution required in CGYRO for typically drift-ballooning modes. If the eigenfunction is visualized in the radial space, each poloidal harmonic is clearly separated by $1/(k_y |s|) \sim 6\rho_s$ as shown in Fig. 4(d), instead of forming an envelope through toroidal coupling[36] as most ballooning-type modes will do, suggesting that this MTM branch has a slab-like character. The bloch angle θ_0 is set to be zero in all the calculations across this paper. Interestingly, the MTM has its eigenfunction (especially $A_\parallel$) mainly peaked on the high field side as shown in Fig. 5. The mode frequency is quite close to the

electron diamagnetic frequency $\omega_{*,pe} = k_y \rho_s (a/L_{T_e} + a/L_{n_e})$ (Fig. 4(e)), which is consistent with the MTM theory as well[34, 37]. For the nominal experimental parameters, the mode is found to be linearly unstable across the range $k_y \rho_s = [0.1, 0.3]$ (Fig. 4(f)).

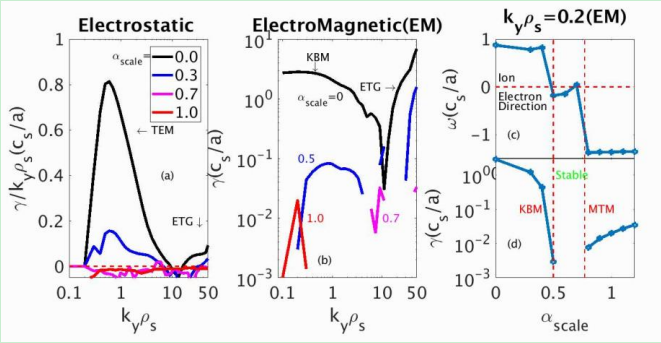

Figure 3. The $\gamma / k_y \rho_s$ (where γ is the linear growth rate) of the electrostatic instabilities (a) and γ of the electromagnetic run (b) for different α_{scale}. The frequency (c) and growth rate (d) of dominant electromagnetic instability of $k_y \rho_s = 0.2$ versus α_{scale} (figure 3(a),(c),(d) reproduced with permission from Phys. Rev. Lett. 123, 22 (2019) [20] Copyright 2019, American Physical Society)

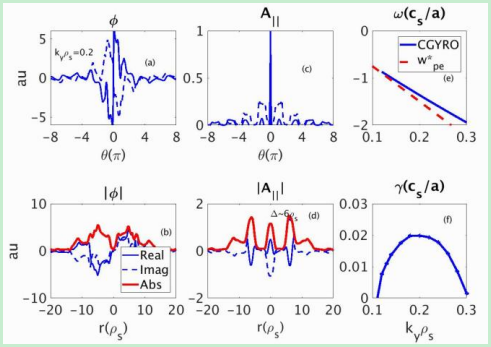

Figure 4. The eigenfunction of ϕ (a&b) and $A_{||}$ (c&d) of $k_y \rho_s = 0.2$ in both the ballooning and radial space. The spectrum of frequency(e) and growth rate(f) of MTM, (figure 4(c)(d)(e)(f) reproduced with permission from Phys. Rev. Lett. 123, 22 (2019) [20] Copyright 2019, American Physical Society)

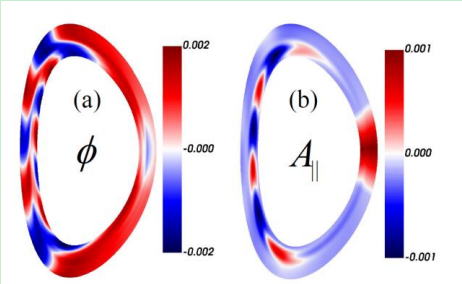

Figure 5. Eigenfunction of ϕ (left panel) and $A_{\parallel}$ (Right Panel) in the RZ space of $k_y\rho_s$ =0.2. For simplicity, the plot is done with toroidal mode number of n =1

Some parametric dependencies of the mode are shown in Fig. 6 to verify and further understand the nature of the instability. The increase of both a/L_{T_e} and β_e (Fig. 6(a) and (b)) are favorable for the destabilization of such a mode, indicating that it is an electromagnetic mode destabilized by a/L_{T_e}, consistent with MTM characteristics. The growth rate exhibits a non-monotonic dependence on the collisionality, maximizing when the collisionality is comparable to the mode frequency, which is also consistent with MTM theory[37] (Fig 6(c)). Furthermore, it is also shown that the growth rate is symmetric about s=0 (Fig. 6(e)), both higher q (Fig. 6(g)) and lower $|s|$ (Fig. 6(e)) are efficient for the mode's excitation, suggesting it to be a slab mode which can be destabilized by reducing $|k_{\parallel}|$ (with $|k_{\parallel}| \sim k_y|s|/q$). Perhaps not commonly known, this MTM can be destabilized by α[38], which makes it greatly different from conventional drift-ballooning modes such as TEMs and KBMs. We note that when scanning those parameters that determine α, such as β_E, a/L_{T_e} and q, α is held fixed to the experimental value to exclude the contribution of its variation to the growth rate, enabling the direct dependence of the mode on those other parameters to be identified. In order to quantify the relative growth rate dependence on different parameters, we define the growth rate sensitivity in Eqn. (1)

$$sensitivity = \frac{x_0}{\gamma_0}\frac{d\gamma}{dx}\bigg|_{x_0} \tag{1}$$

where x_0 and γ_0 are the experimental value of one specific parameter and the growth rate evaluated at x_0, respectively. The sensitivity of the growth rate to each parameter is listed in Table III. As can be seen, the growth rate is only moderately sensitive to β_E and a/L_{T_e}, both of which are commonly identified as key parameters controlling MTM growth. Instead, this MTM branch is found to be most sensitive to s and q, indicating the importance of $k_{\parallel}$ in regulating the mode behavior, which is consistent with a slab-like mode nature. Most notably, if the α effect is self-

consistently considered in the q scan (β^* is unchanged while the dependence of drift frequency on q is shown in Eqs. 109 and 136 in Ref[27]), the sensitivity of q will reach 4.9, which is significantly larger than that of any other parameters.

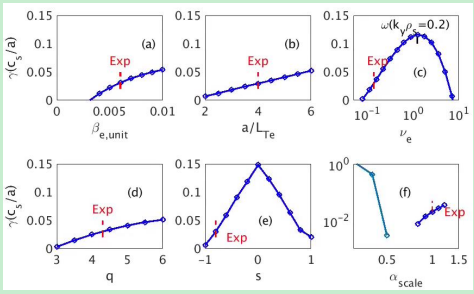

Figure 6 Parametric dependence of the growth rate of $k_y\rho_s = 0.2$ on the (a) $\beta_{E,unit}$; (b) a/L_{T_e}, (c) ν_e, (d) q, (e) s and (f) α_{scale} (Figure 6 reproduced with permission from Phys. Rev. Lett. 123, 22 (2019) [20]
Copyright 2019, American Physical Society)

Table III, The MTM sensitivity

Parameter	s	q	α	ν_e	$\beta_{E,unit}$	a/L_{T_e}
Sensitivity	3.6	2.4	2.1	1.7	1.6	1.5

3.2 Nonlinear microtearing mode simulation results

Having determined that this novel MTM is the only local linearly unstable mode for the experimental parameters of interest, we next examine its nonlinear dynamics, also through gyrokinetic simulation with the CGYRO code. For these nonlinear studies, we employ 24 toroidal mode numbers and 120 radial mode numbers; other grids and physics settings are the same as for the linear analysis described above. The default mode numbers spacings are chosen to be $\Delta k_x\rho_s = 0.2$ and $\Delta k_y\rho_s = 0.08$, such that (L_x , L_y) = (31 ρ_s , 78 ρ_s), where L_x and L_y are the radial and binormal length, respectively. All nonlinear simulations were performed on the CORI machine at NERSC. A typical simulation utilized 9216 cores and generally required 24 – 48 hours to achieve sufficiently well-converged time averaging statistics.

The default radial wavenumber grid choices described above correspond to a grid resolution of $\Delta x/\rho_s \sim 0.25$ (similar to the resolution used in Guttenfelder *et al.*[39]), equivalent to a maximum $k_{x\ s}$ of 11.8. Time traces of the predicted nonlinear energy fluxes are shown in Fig. 7. In order to verify that the mode has been sufficiently radially resolved, a simulation with a 60% increase in

the number of radial grid numbers, which corresponds to $\Delta x / \rho_s$=0.15 and $k_{x,\max}\rho_s$ =19.0, was performed and the result plotted as well in Fig. 7. Both the time traces (Fig. 7(a)) and nonlinear energy flux spectra (Fig. 7(b)) for these cases show very good agreement, demonstrating that $k_{x,\max\ s}$ =11.8 is sufficient for resolving the fine radial structure of the MTM turbulence in the nonlinear simulations. Moreover, we also note (but do not show) that the fluctuation spectra fall off smoothly with radial wavenumber in both cases, without any evidence of high-k_x pileup that would suggest insufficient radial resolution.

As would be expected for MTM turbulence, and consistent with the experimental power balance analysis, the nonlinear simulation predicts only meaningful levels of electron energy flux Q_e are driven, with essentially zero ion energy flux Q_i (Fig. 7(a))[40, 41]. Moreover, almost all of Q_e comes from the magnetic flutter component (i.e. due to $A_\parallel$ fluctuations) while the contributions from ϕ and $B_\parallel$ fluctuations are found to be negligible (Fig. 7(b)), also consistent with MTM characteristics. The nonlinear flux and fluctuation spectra exhibit several notable characteristics. First, significant transport and fluctuation power are observed at the longest wavelengths when simulating the nominal experimental parameters. Additional convergence details for this feature at these parameters are discussed below, and the impact of variations in experimental parameters in the next sub-section. We also recall that the linear unstable range of MTM is $k_y\rho_s$ = [0.1,0.3] while the flux spectrum greatly exceeds such a range (Fig. 7(b)), indicating that a rule of simple mixing-length type will not be able to reproduce the nonlinear flux or spectrum. A similar extension of MTM transport to wavelengths beyond the linear instability range was observed in previous simulations using the GENE code by Doerk[42] *et al***.** Further development of reduced transport models[43, 44] is therefore likely needed to correctly describe these MTM characteristics. Towards this end, it is interesting to observe that the mean frequency of the nonlinear fluctuations as a function of $k_y\rho_s$ closely tracks the linear dispersion relation (Fig. 6(d)), suggesting some key linear mode characteristics are still retained in the nonlinear dynamics. The nonlinear frequency shown here is an averaged frequency determined by averaging the imaginary part of $d(\ln\phi)/dt$ over both radial and poloidal space. A more detailed spectral analysis confirms that the turbulence is dominated by a single mode with well-defined dispersion relation corresponding to the linear MTM prediction, further evidence that the MTM is the key instability for these conditions.

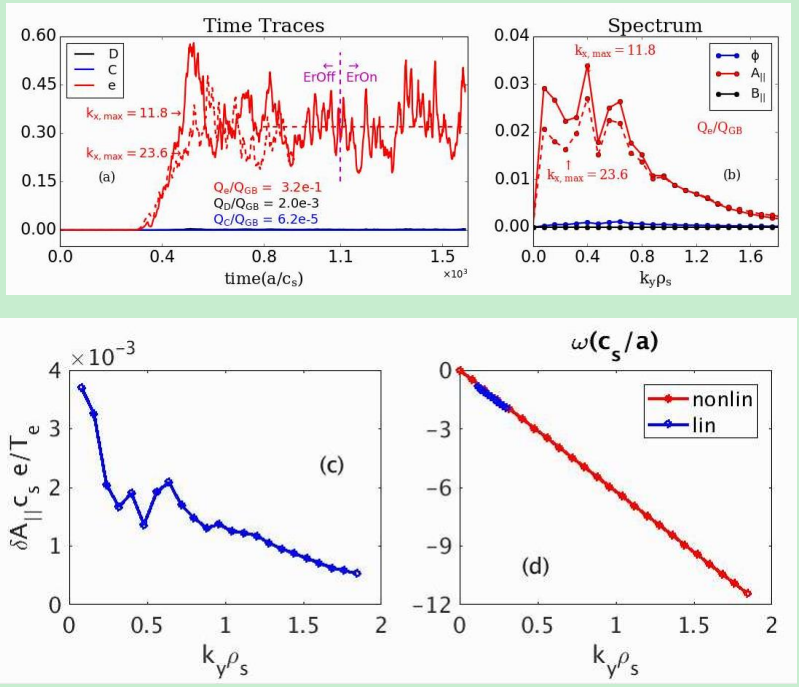

Figure 7 (a)The trace traces of the gyrobohm normalized energy flux of different species, 'D', 'C' and 'e' represent deuterium, carbon, and electron, respectively. (b) The energy spectrum of Q_e induced by different fields. (c) the nonlinear intensity spectrum of $A_{\parallel}$ ($k_y\rho_s = 0$ component has a value of 0.017); (d) comparison between the linear and nonlinear frequency of MTM (Figure 7 (a) (b) reproduced with permission from Phys. Rev. Lett. 123, 22 (2019) [20] Copyright 2019, American Physical Society)

For the case shown in Fig. 7, equilibrium E_r shear (at the nominal experimental level) is included only after 1090 a/c_s. Although this shearing rate (γ_E ~0.08) is much larger than the maximum growth rate of MTM ($\gamma_{MTM,\max}$ ~ 0.02), virtually no impact is observed on predicted transport levels. This insensitivity to strong E_r shear (relative to peak growth rate) is also reported in the recently pedestal MTM work done by Hatch *et al* [45] and Pueschel[46] *et al*, which differ significantly from previous MTM studies by Doerk *et al.* [47, 48] and Guttenfelder *et al.*[39, 49], both of which found significant reductions or suppression of MTM transport at comparable equilibrium shear to maximum growth rate ratios. The response to E_r shear is determined by the shapes of MTM eddies. To illustrate this argument, visualizations of fluctuating electrostatic and magnetic

potentials at $t = 800\, a/c_s$ (Fig. 8 a&b when E_r shear is off) and $t = 1450\ a/c_s$ (Fig. 8 c&d when E_r shear is on) in the (R, Z) plane are shown in Fig. 8. The strong axisymmetric (toroidal mode number $n = 0$) component is removed for better visualization of the finite-n fluctuations that drive the cross-field transport fluxes. As can be seen, the eddies in both ϕ and $A_\parallel$ are always radially narrow and poloidally extended, which is consistent with linear eigenfunctions shown in Fig. 4 and Fig 5. This structure is particularly different from either the streamer-like linear eigenmodes of typical ballooning instabilities or the much more isotropic eddies typically observed in nonlinear simulations of those instabilities, e.g. in simulations of ITG turbulence. The narrow radial extent of these MTM fluctuations likely makes them more resistant to the shearing that can suppress ballooning-type modes through radial decorrelation of the fluctuations [32, 41, 50-52]. However, this mechanism should be investigated further, including a more detailed consideration of other unusual aspects of the MTM in these conditions. Most notably, for these parameters that the MTM localizes in the high field side on the plasma, consistent with previous studies investigating instabilities and turbulence at high kinetic gradient physics[53, 54]. Beyond any impacts this localization might have on the efficiency of equilibrium shear suppression, it presents unique challenges for experimental validation. Most commonly-used core turbulence diagnostics on DIII-D and elsewhere (such as beam emission spectroscopy[55], Doppler backscattering[56, 57], and correlation electron cyclotron emission[58]) focus on low-field-side fluctuations, and will therefore likely not see strong signs of these high-field-side MTMs. However, it should be noted that the density and temperature fluctuations have poloidal distributions more like the electrostatic potential ϕ than $A_\parallel$ (also B_r, which mainly locates at HFS as well), with potentially less localization to the high field side. Additionally, new diagnostics such as the recently deployed DIII-D radial interferometer polarimeter[59] and cross-polarization scattering system[60] may offer a potential route to their measurement in future carefully designed experiments. One could also conceivably use the absence of measured fluctuations as a means of experimentally discriminating between these predictions and those from reduced turbulent transport models such as TGLF or CDBM[61] which are built and calibrated to an assumption of transport driven by low-field-side ballooning instabilities.

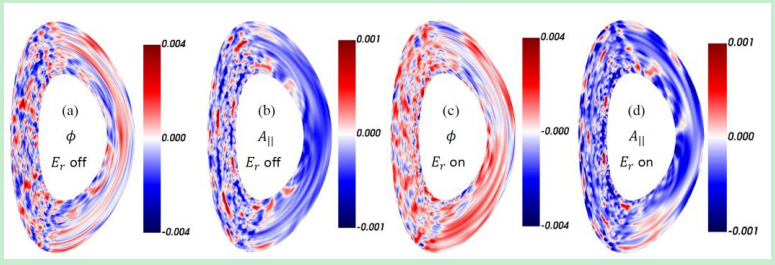

Figure 8. ϕ and $A_{\parallel}$ fluctuation of the MTM turbulence when E_r shear is off (a&b) and on(c&d). Only finite-n fluctuations are plotted.

3.3 Verification and convergence testing of nonlinear results

To ensure these results are computationally robust, a variety of convergence tests have been carried out, in addition to the linear convergence testing described above. In CGYRO, the radial box length unit for nonlinear simulation is $L_{x0} = \dfrac{1}{\Delta k_y \rho_s \,|\, s \,|}$, the radial box length $L_x = n_{bm} L_{x0}$, where n_{bm} is called the box multiplier. A value of n_{bm} = 2 is used for the simulations above, and a convergence test for different n_{bm} values with $k_{x,\max}$~12 fixed (by scaling radial grids accordingly) was performed. The results are shown in Fig. 9(a). As can be seen, n_{bm} of 2 and 5 show similar flux spectra, indicating good convergence is achieved for the radial box size.

Now turning to convergence in binormal box size L_y ($L_y = 2 \,/\, k_y$), note that $k_{y,\min}\rho_s = \Delta k_y \rho_s$ in CGYRO and so $k_{y,\min}\rho_s$ and $\Delta k_y \rho_s$ will be used interchangeably in the following context. A series of nonlinear simulations scanning $k_{y,\min}\rho_s$ across values of 0.125, 0.08, 0.06, and 0.05 were performed with $k_{x,\max}\rho_s$ fixed to ~12. The predicted Q_e spectrum under different $\Delta k_y \rho_s$ is shown in Fig. 9(b) and the total Q_e value is summarized in Table IV. The predicted flux is found to continuously increase as $k_{y,\min}\rho_s$ decreases, even as it goes to the longest wavelength (n~1). As a practical matter, we note that $k_y = nq/r$, or in normalized units $k_y \rho_s = nq(a/r)(\rho_s / a)$. For the parameters considered here (q = 4.3, r/a =0.62, ρ_s / a = 5.5e-3), $\Delta k_y \rho_s$ = 0.04 corresponds to toroidal mode number dn = 1, and so physically it would not make sense to go to larger binormal box sizes. Whether global effects and other terms neglected in the standard gyrokinetic equation[62] become important at this point certainly come into question, although we note that the fine radial scales of the turbulence and strong non-ballooning make a quantitative assessment of these terms' impact non-trivial. It should also be noted that the shape of this spectrum is strongly dependent on the magnetic shear used; this point will be further discussed below in Section 3.4.

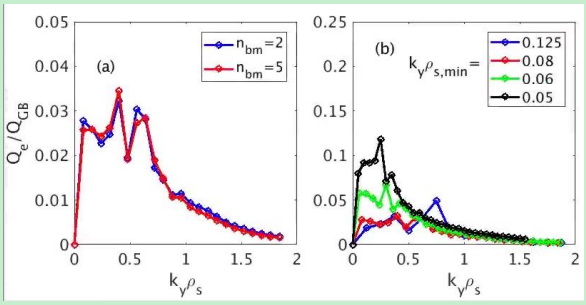

Figure 9. The Q_e flux spectrum versus L_x (a) and L_y (b)

Table IV. Predicted Q_e for different $k_{y,\min}\rho_s$

$k_{y,\min}\rho_s$	0.125	0.08	0.06	0.05
Q_e	0.25± 0.05	0.32±0.06	0.66±0.15	1.13±0.18

3.4 Comparison between nonlinear predictions and experiment

In order to meaningfully compare our simulation predictions to experimental observations, the impact of propagating experimental uncertainties must be considered and quantified as well as numerical convergence tests. Motivated by the linear analysis shown in Fig. 6(e), we focus on assessing the impact of experimental uncertainties in the magnetic shear on the results. The uncertainty in the local magnetic shear is determined via the use of a Monte Carlo approach using the OMFIT EFIT[23, 63] module to calculate an ensemble of magnetic equilibrium reconstructions. The consequently estimated s values at ρ = 0.6 are bounded by two extrema between -1.2 and -0.3 (Fig 10(a)). A set of linear stability calculations covering this range is shown in Fig. 10(b), showing that the linear growth rate of the MTM increases with the decrease of the magnetic shear (i.e. as s goes from -1 to zero). We note that:

(i) all drift-wave modes are confirmed to be stable due to the strong α stabilization within this s range;
(ii) no unstable mode occurs for s < -1.0, therefore only modes of $s \geq$ -0.8 are shown.

The corresponding predicted Q_e increases monotonically with the increase of s (Fig. 10(c)), consistent with the linear stability calculation. In particular, the simulation with $k_{y,\min}\rho_s$ of 0.08 matches the experiment at s = -0.3, which is (barely) within the experimental uncertainties, although we also note that all other parameters have been held fixed, including key MTM drivers such as safety factor q and collisionality υ_e. Also, predicted Q_e values using different $k_{y,\min}\rho_s$

are plotted as well and shown to be scattered around the experimental value (Fig. 10(c)) depending upon the particular shear value used, indicating that the MTM can drive the flux to the experimental inferred level. Based on these results, the expected impact of incorporating additional experimental uncertainties, as well as the robustness of the α-stabilization of non-MTM modes, we identify the MTM as the extremely likely candidate for controlling residual electron energy transport in the ITB region of these discharges. As described above, further validation of these predictions through direct measurement of the MTM fluctuations is likely to be challenging due to their high-field-side localization and strongly anisotropic structure. However, a combination of carefully designed experiments and the utilization of novel diagnostics may offer a path forward.

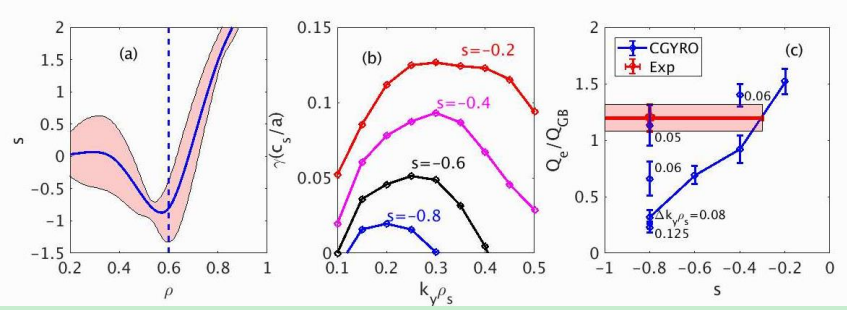

Figure 10. (a) The experimental s profile with uncertainties evaluated from Monte Carlo analysis; (b), linear spectrum of different magnetic shear; (c) Comparison between the CGYRO predicted Q_e and experimental one;(Figure 10 reproduced with permission from Phys. Rev. Lett. 123, 22 (2019) [20] Copyright 2019, American Physical Society)

4. Interpretation of TGYRO results on DIII-D experiments

While the ion thermal transport in these discharges is driven by neoclassical transport as shown in Section 2, the analysis in Section 3 demonstrates that the electron thermal transport is driven by MTMs. We now seek to understand why TGLF is unable to correctly predict the T_e profile as observed in Section 2, and more generally, why TGLF is more likely to incorrectly predict T_e profiles for higher q shots[5, 12]. CGYRO predicts the dominant mode will transit from the trapped electron mode (TEM) to MTM with the increase of q when the α effect is self-consistently considered, as shown in Fig. 11; for this particular case, the experiment lies well-within the MTM domain. Such a transition is reasonable because increasing α (via increasing q) stabilizes the TEM, while both q and α can destabilize the MTM efficiently as discussed in Section 3.1. As a comparison, TGLF is broadly able to reproduce the TEM features when q is low but unable to predict the destabilization of slab-like MTM at higher q in its present version since the Hermite basis functions used in TGLF are not suitable for representing the eigenfunction of the slab MTM. This finding qualitatively explains why TGLF struggles to correctly predict the T_e profile in the

high q regime[5, 12]. It seems that due to the lack of capability in predicting the slab-MTM, TGYRO with TGLF will, therefore, raise the a/L_{Te} to drive stronger ES-DW instabilities to generate the (MTM-induced) missing flux. It should be noted that the MTM is not only unstable at $\rho = 0.6$ as discussed in this paper, but can be the dominant instability across the whole ITB region as shown in Ref. [20]. It is also worth noting that energetic particle driven modes, such as toroidal Alfven eigenmodes, are more likely to be driven unstable at high $q\,(q_{\min})$[64-66] but cannot be resolved in TGLF using the standard resolution. As these modes can drive electron thermal transport (in addition to fast ion transport), they may also contribute to the observation that the TGLF is more likely to fail under higher q shots.

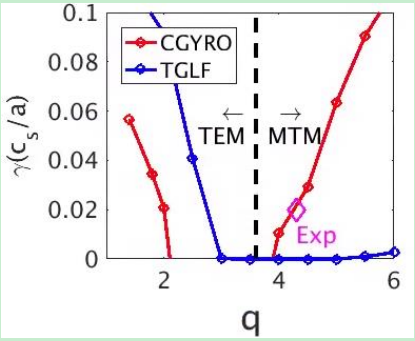

Figure 11. The parametric dependence of the growth rate of dominant mode on q

5. Extrapolation to future burning plasmas

In recent work by McClenaghan *et al.* [67], an integrated modeling study using TGYRO and TGLF was employed to develop a potential high β_p operating scenario for ITER. The predicted density, temperature, and safety factor profiles are shown in Fig. 12. Similar to the DIII-D experimental profiles, a strong large-radius ITB is formed at ρ ~0.65 in both T_i and T_e channels, co-located with a region of negative magnetic shear. One important question regarding this scenario is to determine whether the MTM branch predicted by CGYRO but not TGLF will still exist in the ITER scenario, given the limitations identified in Sec. 4. To connect with the DIII-D analysis, parameters at $\rho = 0.6$, which remains within the ITB region, are chosen to perform a linear stability analysis; specific values are listed in Table V. Fig. 13 shows that the linear calculation between TGLF and CGYRO generally agrees well, with both CGYRO and TGLF predicting the dominant low-k_y ($k_y\rho_s < 1$) instability to be the ITG mode, rather than the MTM mode described above. Although there are some larger discrepancies between the predictions at high-k_y, TGLF predicts the low-k_y region will be the dominant source of transport and multiscale effects to be unimportant. At one level, this prediction can be understood by examining the linear

spectrum plot shown in Fig. 13, the $\gamma / k_y \rho_s$ spectrum is significantly larger in the low-k_y region compared to the high-k_y region, whereas recently studies[25,61] have identified peaking in the high-ky region as a critical indicator of multiscale effects playing an important role. Alternatively, one can view the situation through the "fingerprint" paradigm advocated in e.g. Kotschenreuther *et al*[41] and Hatch *et al*[68]. From this perspective, one first notes that the inherently smaller collisionality of ITER relative to DIII-D will very likely render ion neoclassical transport too small to drive the expected levels of ion thermal transport, and so a self-consistent solution inherently must have sufficient long-wavelength turbulence capable of driving the "needed" amount of Q_i. In either case, the question then becomes what other parameters or physics have changed to drive the fundamentally different microinstabilities between the DIII-D and ITER high β_p plasmas, as the local stability analysis is independent of the difference in normalized gyroradius between the machines.

If we compare the parameters listed in Tables II and V, it is clear that except for the higher a / L_{T_e} value, more parameters are changing in the direction of MTM suppression from DIII-D to ITER, like higher $|s|$, lower q, $\beta_{E,unit}$, α and most importantly, much lower collisionality. Moreover, due to the high fueling efficiency of the neutral beam injection (NBI) in DIII-D tokamak, the strong ITB in the density channel normally coexists with the temperature channel ($a / L_{n_e,DIII-D} \sim 3.4$). However, core fueling is expected to be significantly weaker for ITER and thus the density gradient is quite low even in the ITB region ($a / L_{n_e,ITER} \sim 0.6$). Consequently, the η values (defined as $\eta = L_n / L_T$), for which large values are favorable for driving the ES-DW instabilities, are expected to be much higher in the ITER scenario.

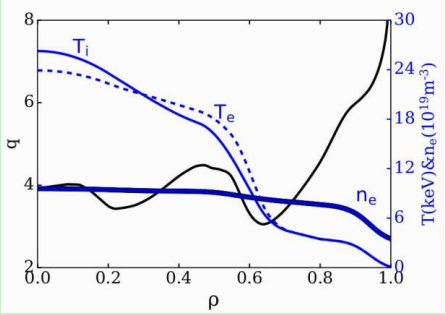

Figure 12. The q profile and kinetic profiles of the predicted ITER high β_p scenario[67]

Table V, Parameters of $\rho_{tor} = 0.6$ of the ITER scenario

r/a	R/a	a/L_{Te}	a/L_{T_i}	a/L_{n_e}	T_e/T_i

0.62	3.3	8.3	7.3	0.63	0.83
s	q	$\beta_{E,unit}$	α	γ_E	ν_e
-2.30	3.3	4.4e-3	2.3	0	0.013

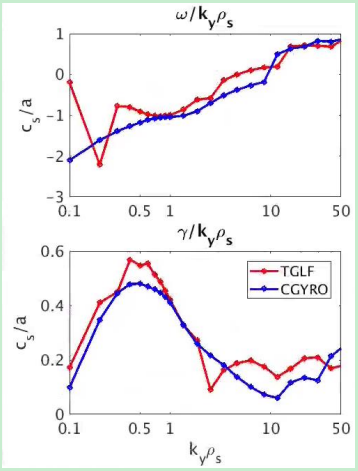

Figure 13. Comparison between TGLF and CGYRO electromagnetic linear calculation of ρ_{tor} = 0.6 of the ITER scenario with Debye length effect considered

To further quantify these transitions, scalings of the MTM and ITG growth rates with collisionality ν and scale length ratio η are shown in Fig. 14, using all other parameters from the DIII-D conditions described above. The growth rate of MTM versus collisionality is shown in Fig. 14(a). As can be seen, the DIII-D collisionality is able to excite MTMs while the MTM is robustly stable under the ITER relevant collisionality. Note that we do not exclude the possibility of collisionless MTM excitation if even lower collisionality can be achieved. To understand the physics changes that destabilize the ITG mode in ITER, we first note that beyond the significantly larger value of a/L_{T_i} in the ITER case, the α effect is very important for the suppression of drift-waves and ballooning modes as discussed in section 3.1. Additionally, high density gradients, which can reduce the η value, also contribute to the full stabilization of drift-waves for the DIII-D scenario. To quantify this dependence, we examine the variations in predicted growth rate by scaling up and down the temperature and density gradients, respectively, while keeping the total pressure gradient(α) fixed, to examine the role of the density gradient in controlling the DW instabilities. The corresponding result is shown in Fig 14(b). As can be seen, while the ITG is stable at DIII-D η_i, ITER η_i value, which is much higher, can destabilize the ITG. From this perspective, we, therefore, can have some increased confidence in being able to realize the scenario

developed in Ref. [67] in ITER, because it is more likely to lie in the region where ITG and other conventional ballooning instabilities dominate transport, rather than the MTM which controls the DIII-D scenario.

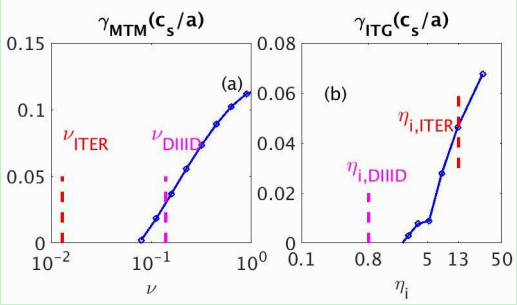

Figure 14 (a) the growth rate of MTM versus collisionality under DIII-D; (b) the growth rate of ITG versus ITG. Both (a) and (b) are based on the DIII-D background parameters

However, we should exercise caution in generalizing the success of this specific case to future high β_p scenarios in general. The reason is that while the slab-like MTM mode discussed in this paper will disappear due to reduced collisionality, theory[69] also predicts that a slab branch of ES-DW, which is not able to be suppressed by the high α, may exist and even dominate when the α is high enough to make the value of $\omega_d / k_\parallel v_T$ sufficiently small (here ω_d is the magnetic drift frequency). This prediction can be verified by looking at the dependence of mode behavior on local safety factor q_{loc} (with the α value changed self-consistently) as shown in Fig. 15. In this analysis, all the background parameters (including the geometry, kinetic and magnetic parameters, etc) are taken from ρ_{tor} =0.6 of the ITER scenario. Here, CGYRO predicts the dominant mode will transit from a conventional ballooning-type mode to a slab mode with an increase of q_{loc}. Again, TGLF can roughly reproduce the α stabilization of the conventional branch, but unfortunately, it is not able to resolve the slab branch with its standard resolution. The eigenfunctions predicted by CGYRO and TGLF under different q_{loc} are shown in Fig 16. CGYRO predicts the dominant mode under high q_{loc} is a slab one with its eigenfunction peaking at the high field slide (Fig. 16 (c)) while TGLF still predicts a ballooning-type one under the same q_{loc} (Fig. 16 (f)). Given that the basis functions used by TGLF to calculate eigenmodes are optimized for typical ballooning instabilities, and that TGLF was not calibrated to nonlinear simulations near this regime of parameter space, this divergence between TGLF and CGYRO is not unexpected. While this transition may occur at higher local values of q than may be expected in an ITER ITB, the underlying physics may well be relevant both for predicting stability in the pedestal region (which will have higher q_{loc}, α, and collisionality) as well as other future reactors with different

shapes and/or geometries, such as spherical tokamaks. In general, the higher the safety factor in the scenario, the more care must be taken in extrapolating current experimental results and reduced model predictions to future burning plasma regimes.

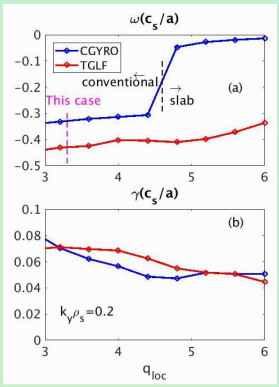

Figure 15. Comparison of frequency(a) and growth rate(b) between TGLF and CGYRO prediction versus the local q under the ITER parameters ($\rho_{tor} = 0.6$). α is changed self-consistently with q_{loc}.

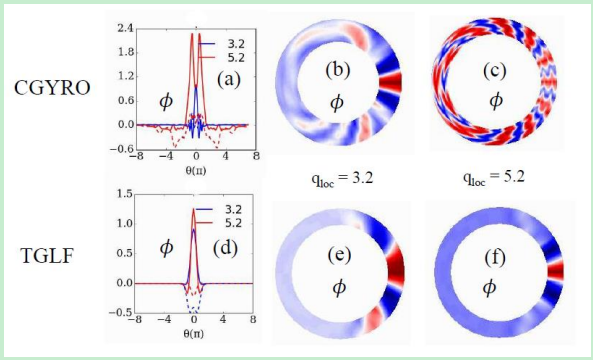

Figure 16. Eigenfunctions of ϕ ($k_y\rho_s = 0.2$) under different q_{loc} in the ballooning space output by CGYRO (a) and TGLF(d). The eigenfunction in the RZ space output by CGYRO (b&c) and TGLF (e&f) under different q_{loc}. For simplicity, the RZ plots here are based on circular geometry.

6. Conclusion

Understanding the sources of anomalous electron energy transport in ITBs and other regions where ion energy transport has been reduced to neoclassical[20] levels has been a long-standing challenge within tokamak transport research. Resolving this question is particularly important for accurately extrapolating the high β_p scenario to future devices such as ITER. In this work,

through dedicated linear and nonlinear gyrokinetic calculations using CGYRO, an MTM instability is shown to drive the electron energy transport in the ITB region of DIII-D high β_p plasmas. This MTM has several novel properties, listed below.

(i) The eigenfunction of MTM is highly extended in the ballooning space with multiple harmonics, which makes the eigenfunction in the radial space 'separated' for each poloidal harmonic and is therefore identified to be a slab mode;
(ii) The MTM growth rate is most sensitive to q and s, consistent with its slab nature. Its dependence on the a/L_{Te} and β_E, which are believed to be the main drive for MTM, is only moderate;
(iii) The α effect, which is typically stabilizing for conventional ES-DW, destabilizes the slab MTM whose eigenfunction mainly peaks at the high field side. The MTM is the only micro-instability under experimental parameters and is shown to be able to drive experimental relevant flux by nonlinear CGYRO simulation;
(iv) The nonlinear electron energy flux spectrum extends well beyond the range of linearly unstable wavenumbers, which differs from conventional ES-DW instabilities as well;
(v) Nonlinearly, eddies of the MTM are radially narrow and poloidal extended, which is very different from the conventional ES-DW turbulence and makes it insensitive to the strong E_r shear in the ITB region.

A key consequence of these novel properties is that this MTM branch is not captured by TGLF, which appears to be a likely reason that transport modeling using TGLF overpredicts the T_e profile for high β_p scenarios with large safety factor q. However, the MTM is unlikely to be able to regulate the T_e profile in a future device such as ITER due to the significantly lower collisionality expected there. Analysis of an ITER high β_p scenario developed using TGLF found that both CGYRO and TGLF predicted the ITG mode to be dominant in the ITB region, with relatively good agreement in growth rates for those parameters. Beyond the difference in collisionality, the ITER scenario has both lower a/L_{n_e} and higher a/L_{T_i} which further favors destabilization of the ITG mode. Intuitively, this change in dominant instability is not unexpected if one notes that neoclassical ion energy transport is expected to be significantly smaller in ITER than in DIII-D conditions, which therefore requires an instability capable of driving ion energy transport to be unstable in a self-consistent scenario. The upshot is that although the ITBs in the ITER and DIII-D high β_p scenarios are predicted to be governed by different transport processes, TGLF appears to be better suited for the ITER case than for the DIII-D conditions.

Looking beyond the specific ITER scenario considered here, we would note that while the particular MTM branch discussed here is unlikely to persist in the core of future devices, it may be relevant for modeling pedestal transport in those machines (which will have large α and higher

q values, as well as significantly higher collisionality than the core). More broadly, our analysis suggests that a range of other electrostatic and electromagnetic slab-like modes localizing to the high-field side can be destabilized at large α for reactor-like conditions. Like the MTM discussed here, these instabilities are unlikely to be captured by TGLF, or other reduced transport models[70-72] which assume a typical ballooning-like structure for the turbulence. Therefore, it will be extremely important to verify scenarios for future reactors developed with reduced models against gyrokinetic predictions, especially if those scenarios rely on strong α stabilization to obtain the needed confinement level. The future study of these instabilities and their nonlinear dynamics represents a new facet to the rich array of unconventional physics exhibited by plasma turbulence at high driving gradients. Also, global treatment for the ITB region for the ITER case should be performed by utilizing the recent development of CGYRO global capability[73].

Acknowledgments: Discussions with W. Guttenfelder, D.R. Hatch, M.J. Pueschel, M. Kotschenreuther, and H. Xie are appreciated. Technical support from S.Smith, K-J.Kim and M-Q. Wu is also greatly appreciated. This work was supported by the U.S. Department of Energy under awards DE-SC0018287, DE-SC0017992, DE-FG02-95ER54309 and DE-FC02-04ER54698.The data that support the findings of this study are available from the corresponding author upon reasonable request.

References

1. K. Ikeda, in *Nuclear Fusion* (2007), Vol. 47.
2. A. M. Garofalo, X. Gong, B. A. Grierson, Q. Ren, W. M. Solomon, E. J. Strait, M. A. Van Zeeland, C. T. Holcomb, O. Meneghini and S. P. Smith, Nuclear Fusion **55** (12), 123025 (2015).
3. T. Fujita, S. Ide, Y. Kamada, T. Suzuki, T. Oikawa, S. Takeji, Y. Sakamoto, Y. Koide, A. Isayama and T. Hatae, Physical Review Letters **87** (8), 085001 (2001).
4. T. Fujita, S. Ide, H. Shirai, M. Kikuchi, O. Naito, Y. Koide, S. Takeji, H. Kubo and S. Ishida, Physical review letters **78** (12), 2377 (1997).
5. S. Ding, A. Garofalo, J. Qian, L. Cui, J. McClenaghan, C. Pan, J. Chen, X. Zhai, G. McKee and Q. Ren, Physics of Plasmas **24** (5), 056114 (2017).
6. Q. Ren, A. Garofalo, X. Gong, C. Holcomb, L. Lao, G. McKee, O. Meneghini, G. Staebler, B. Grierson and J. Qian, Physics of Plasmas **23** (6), 062511 (2016).
7. J. Huang, X. Gong, A. Garofalo, J. Qian, J. Chen, M. Wu, M. Li, Q. Yuan, L. Wang and C. Pan, Plasma Physics and Controlled Fusion **62** (1), 014019 (2019).
8. J. McClenaghan, A. Garofalo, L. Lao, D. Weisberg, O. Meneghini, S. Smith, B. Lyons, G. Staebler, S. Ding and J. J. N. F. Huang, **60** (4), 046025 (2020).

9. C. Bourdelle, G. Hoang, X. Litaudon, C. Roach, T. Tala and I. I. D. W. Group, Nuclear Fusion **45** (2), 110 (2005).
10. M. A. Beer, G. Hammett, G. Rewoldt, E. Synakowski, M. Zarnstorff and W. Dorland, Physics of Plasmas **4** (5), 1792-1799 (1997).
11. T. Tala, F. Imbeaux, V. Parail, C. Bourdelle, G. Corrigan, X. Garbet, D. Heading, X. Litaudon, P. Strand and J. Weiland, Nuclear Fusion **46** (5), 548 (2006).
12. J. McClenaghan, A. M. Garofalo, O. Meneghini, S. P. Smith, J. A. Leuer, G. M. Staebler, L. L. Lao, J. M. Park, S. Y. Ding and X. Gong, Nuclear Fusion **57** (11), 116019 (2017).
13. J. Candy, C. Holland, R. Waltz, M. R. Fahey and E. Belli, Physics of Plasmas **16** (6), 060704 (2009).
14. E. Belli and J. Candy, Plasma Physics and Controlled Fusion **54** (1), 015015 (2011).
15. E. Belli and J. Candy, Plasma Physics and Controlled Fusion **50** (9), 095010 (2008).
16. G. Staebler, J. Kinsey and R. Waltz, Physics of Plasmas **12** (10), 102508 (2005).
17. G. Staebler, J. Kinsey and R. Waltz, Physics of Plasmas **14** (5), 055909 (2007).
18. M. Shimada, D. Campbell, V. Mukhovatov, M. Fujiwara, N. Kirneva, K. Lackner, M. Nagami, V. Pustovitov, N. Uckan and J. Wesley, Nuclear Fusion **47** (6), S1 (2007).
19. G. Zhuang, G. Li, J. Li, Y. Wan, Y. Liu, X. Wang, Y. Song, V. Chan, Q. Yang and B. Wan, Nuclear Fusion **59** (11), 112010 (2019).
20. X. Jian, C. Holland, J. Candy, E. Belli, V. Chan, A. M. Garofalo and S. Ding, Physical review letters **123** (22), 225002 (2019).
21. V. Chan, A. Costley, B. Wan, A. Garofalo and J. Leuer, Nuclear Fusion **55** (2), 023017 (2015).
22. E. Synakowski, S. Batha, M. Beer, M. Bell, R. Bell, R. Budny, C. Bush, P. Efthimion, G. Hammett and T. Hahm, Physical Review Letters **78** (15), 2972 (1997).
23. O. Meneghini, S. Smith, L. Lao, O. Izacard, Q. Ren, J. Park, J. Candy, Z. Wang, C. Luna and V. Izzo, Nuclear Fusion **55** (8), 083008 (2015).
24. J. Kinsey, G. Staebler and R. Waltz, Physics of Plasmas **15** (5), 055908 (2008).
25. G. M. Staebler, J. Candy, N. T. Howard and C. Holland, Physics of Plasmas **23** (6), 062518 (2016).
26. J. Candy, E. Belli and R. Bravenec, Journal of Computational Physics **324**, 73-93 (2016).
27. J. Candy, Plasma Physics and Controlled Fusion **51** (10), 105009 (2009).
28. R. Miller, M. Chu, J. Greene, Y. Lin-Liu and R. Waltz, Physics of Plasmas **5** (4), 973-978 (1998).
29. H. Sugama, T.-H. Watanabe and M. Nunami, Physics of Plasmas **16** (11), 112503 (2009).
30. A. Garofalo, X. Gong, S. Ding, J. Huang, J. McClenaghan, C. Pan, J. Qian, Q. Ren, G. Staebler and J. Chen, Plasma Physics and Controlled Fusion **60** (1), 014043 (2017).
31. X. Jian, V. Chan, J. Chen, A. Bock, H. Zohm, E. Fable, W. Guo and G. Zhuang, Nuclear Fusion (2019).
32. W. Horton, Reviews of Modern Physics **71** (3), 735 (1999).
33. W. Tang, J. Connor and R. Hastie, Nuclear Fusion **20** (11), 1439 (1980).
34. J. Drake and Y. Lee, The Physics of Fluids **20** (8), 1341-1353 (1977).
35. D. Hatch, M. Kotschenreuther, S. Mahajan, M. Pueschel, C. Michoski, G. Merlo, E. Hassan, A. Field, L. Frassinetti and C. Giroud, arXiv preprint arXiv:07332 (2020).
36. J. Connor, R. Hastie and J. Taylor, Physical Review Letters **40** (6), 396 (1978).
37. R. D. Hazeltine, D. Dobrott and T. Wang, The Physics of Fluids **18** (12), 1778-1786 (1975).
38. D. Dickinson, C. Roach, S. Saarelma, R. Scannell, A. Kirk and H. Wilson, Plasma Physics and Controlled Fusion **55** (7), 074006 (2013).
39. W. Guttenfelder, J. Candy, S. Kaye, W. Nevins, E. Wang, R. Bell, G. Hammett, B. LeBlanc, D. Mikkelsen and H. Yuh, Physical Review Letters **106** (15), 155004 (2011).
40. J. Chowdhury, Y. Chen and S. E. Parker, Physics of Plasmas **27** (4), 042309 (2020).
41. M. Kotschenreuther, X. Liu, D. Hatch, S. Mahajan, L. Zheng, A. Diallo, R. Groebner, J. Hillesheim, C. Maggi and C. Giroud, Nuclear Fusion **59** (9), 096001 (2019).
42. H. Doerk, F. Jenko, M. Pueschel and D. Hatch, Physical Review Letters **106** (15), 155003 (2011).

43. T. Rafiq, J. Weiland, A. Kritz, L. Luo and A. Pankin, Physics of Plasmas **23** (6), 062507 (2016).
44. T. Xie, M. Pueschel and D. Hatch, Physics of Plasmas **27** (8), 082306 (2020).
45. D. Hatch, M. Kotschenreuther, S. Mahajan, P. Valanju, F. Jenko, D. Told, T. Görler and S. Saarelma, Nuclear Fusion **56** (10), 104003 (2016).
46. M. Pueschel, D. Hatch, M. Kotschenreuther, A. Ishizawa and G. Merlo, Nuclear Fusion **60** (12), 124005 (2020).
47. H. Doerk, F. Jenko, M. Pueschel and D. J. P. r. l. Hatch, **106** (15), 155003 (2011).
48. H. Doerk, F. Jenko, T. Görler, D. Told, M. Pueschel and D. Hatch, Physics of Plasmas **19** (5), 055907 (2012).
49. W. Guttenfelder, J. Candy, S. Kaye, W. Nevins, E. Wang, J. Zhang, R. Bell, N. Crocker, G. Hammett and B. LeBlanc, Physics of Plasmas **19** (5), 056119 (2012).
50. H. Biglari, P. Diamond and P. Terry, Physics of Fluids B: Plasma Physics **2** (1), 1-4 (1990).
51. P. Terry, Review of Modern Physics **72** (1), 109 (2000).
52. W. Horton, Review of Modern Physics **71** (3), 735 (1999).
53. M. Pueschel, D. R. Hatch, D. R. Ernst, W. Guttenfelder, P. W. Terry, J. Citrin and J. Connor, Plasma Physics and Controlled Fusion (2018).
54. H.-s. Xie and B. Li, Physics of Plasmas **23** (8), 082513 (2016).
55. G. R. McKEE, R. J. Fonck, D. K. Gupta, D. J. Schlossberg, M. W. Shafer, R. L. Boivin and W. Solomon, Plasma Fusion Research **2**, S1025-S1025 (2007).
56. W. Peebles, T. Rhodes, J. Hillesheim, L. Zeng and C. Wannberg, Review of Scientific Instruments **81** (10), 10D902 (2010).
57. X. Feng, A. Liu, C. Zhou, X. Zou, G. Zhuang, T. Wang, Y. Liu, S. Wang, Y. Li and T. Shi, Physics of Plasmas **27** (8), 082501 (2020).
58. C. Sung, W. Peebles, C. Wannberg, T. Rhodes, X. Nguyen, R. Lantsov and L. Bardóczi, Review of Scientific Instruments **87** (11), 11E123 (2016).
59. J. Chen, W. Ding, D. Brower, D. Finkenthal, C. Muscatello, D. Taussig and R. Boivin, Review of Scientific Instruments **87** (11), 11E108 (2016).
60. T. Rhodes, K. Barada, W. Peebles and N. Crocker, Review of Scientific Instruments **87** (11), 11E726 (2016).
61. K. Itoh, S.-I. Itoh, A. Fukuyama, M. Yagi, M. J. P. p. Azumi and c. fusion, **36** (9), 1501 (1994).
62. H. Sugama and W. Horton, Physics of Plasmas **5** (7), 2560-2573 (1998).
63. L. Lao, H. S. John, R. Stambaugh, A. Kellman and W. Pfeiffer, Nuclear Fusion **25** (11), 1611 (1985).
64. W. Heidbrink, M. Van Zeeland, M. Austin, E. Bass, K. Ghantous, N. Gorelenkov, B. Grierson, D. A. Spong and B. Tobias, Nuclear Fusion **53** (9), 093006 (2013).
65. R. E. Waltz, E. M. Bass, W. W. Heidbrink and M. A. VanZeeland, Nuclear Fusion **55** (12), 123012 (2015).
66. E. Bass and R. Waltz, Nuclear Fusion **60** (1), 016032 (2019).
67. J. McClenaghan, A. Garofalo, L. Lao, D. Weisberg, O. Meneghini, S. Smith, B. Lyons, G. Staebler, S. Ding and J. Huang, Nuclear Fusion **60** (4), 046025 (2020).
68. D. Hatch, M. Kotschenreuther, S. Mahajan, G. Merlo, A. Field, C. Giroud, J. Hillesheim, C. Maggi, C. P. von Thun and C. Roach, Nuclear Fusion **59** (8), 086056 (2019).
69. J. Y. Kim and W. Horton, Physics of Fluids B: Plasma Physics **3** (5), 1167-1170 (1991).
70. R. Waltz, G. Staebler, W. Dorland, G. Hammett, M. Kotschenreuther and J. Konings, Physics of Plasmas **4** (7), 2482-2496 (1997).
71. K. Itoh, S.-I. Itoh, A. Fukuyama, M. Yagi and M. Azumi, Plasma Physics and Controlled Fusion **36** (9), 1501 (1994).
72. M. Kotschenreuther, W. Dorland, M. Beer and G. Hammett, Physics of Plasmas **2** (6), 2381-2389 (1995).

73. J. Candy, E. Belli and G. Staebler, Plasma Physics and Controlled Fusion **62** (4), 042001 (2020).

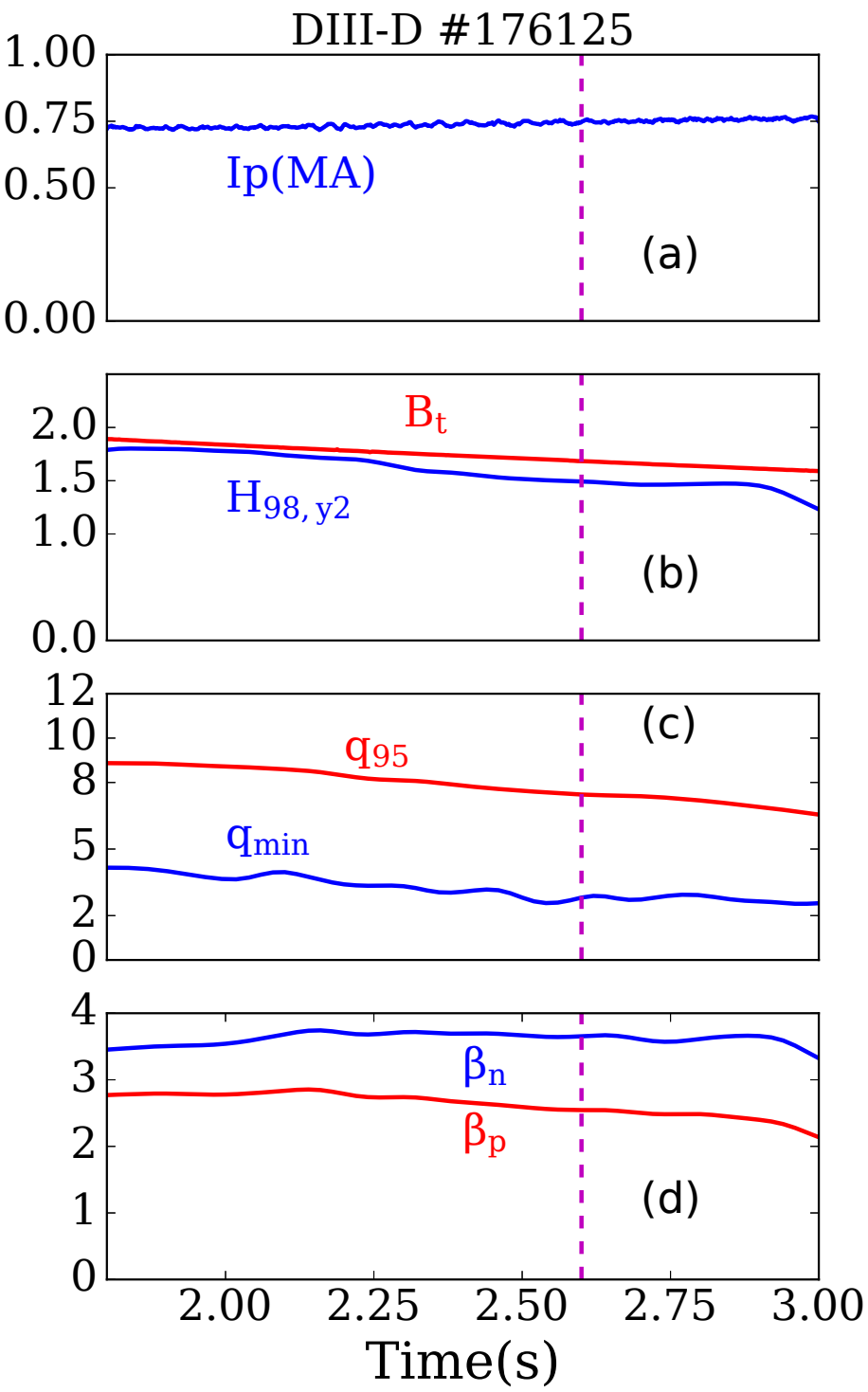

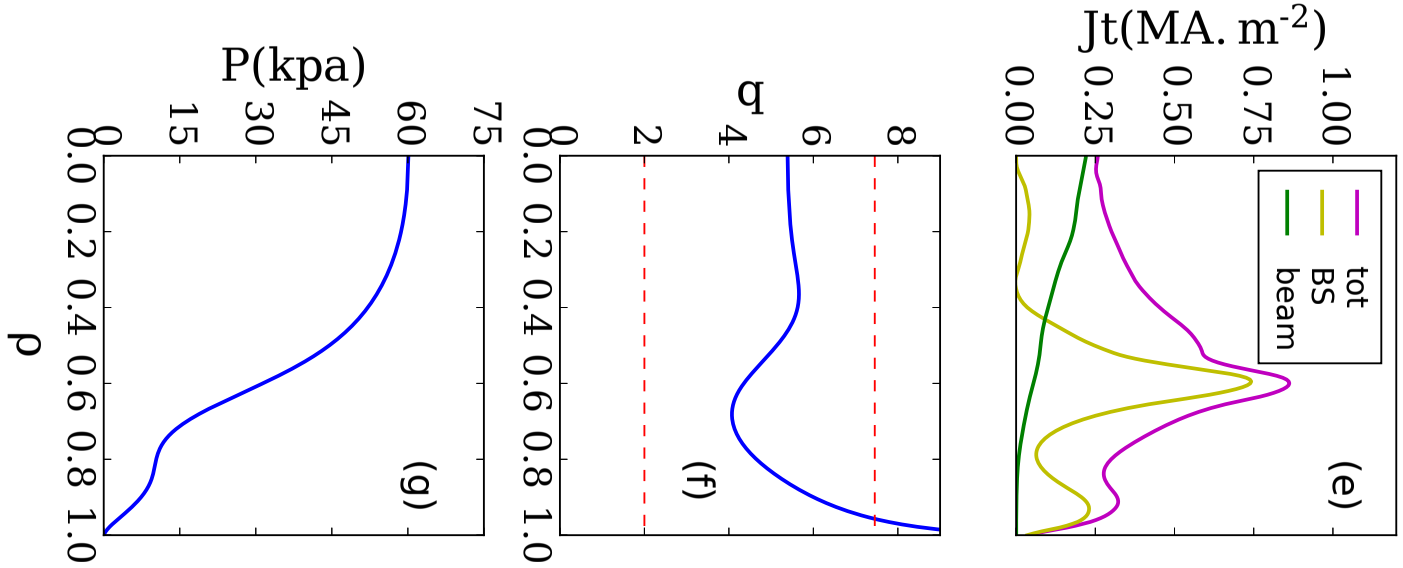

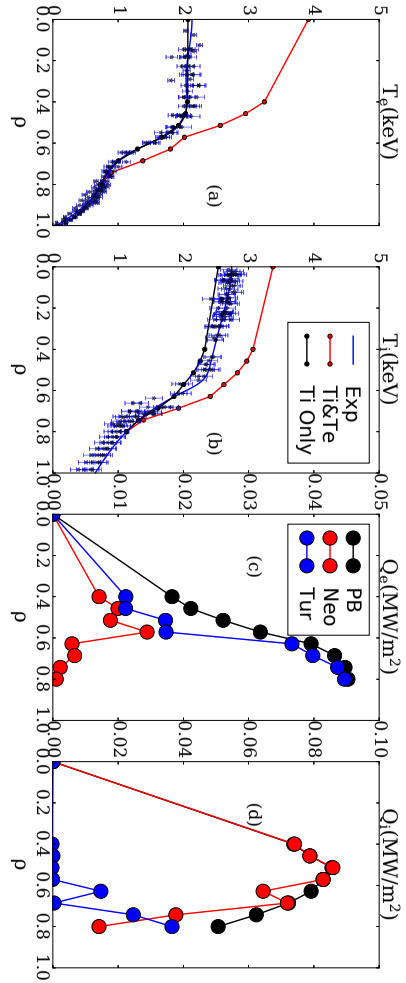

Physics of Plasmas

PLEASE CITE THIS ARTICLE AS DOI: 10.1063/5.0037246

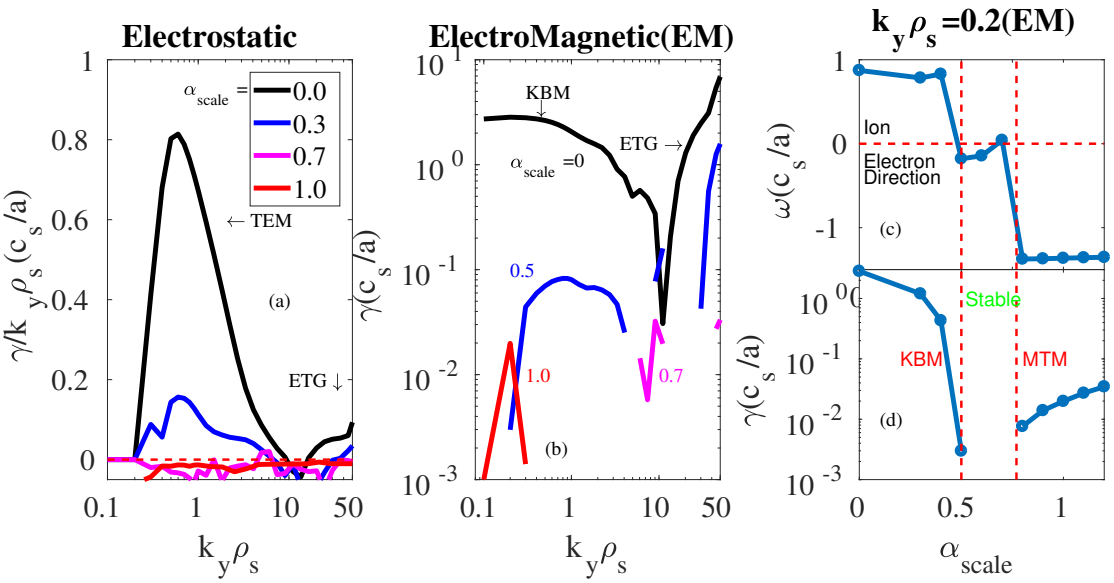

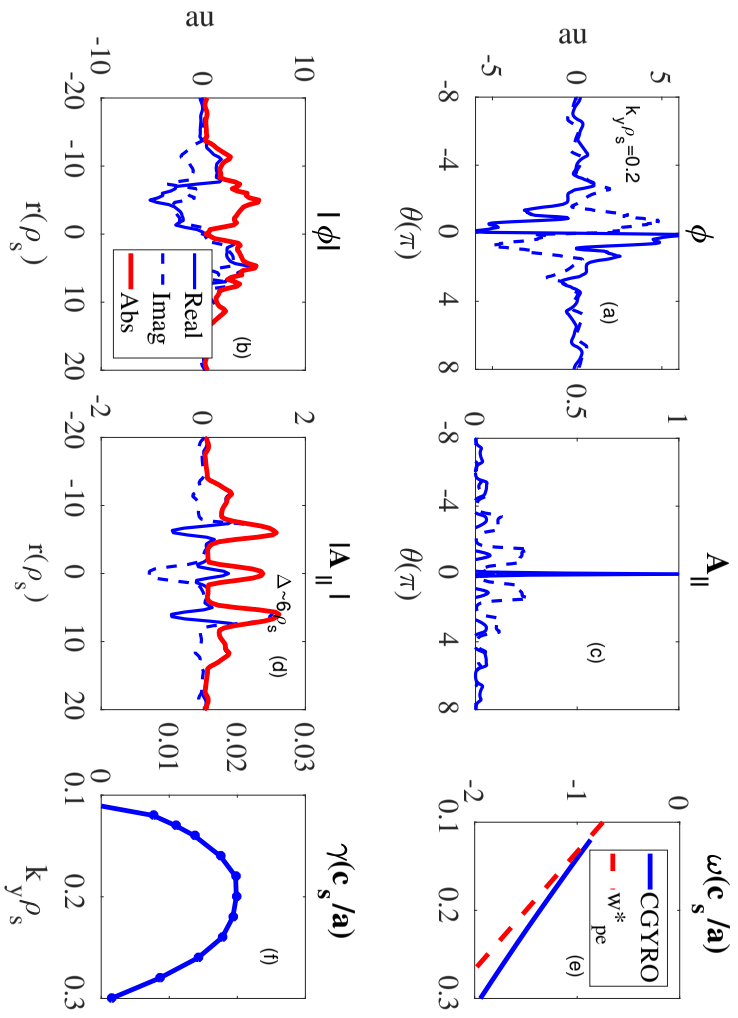

PLEASE CITE THIS ARTICLE AS DOI: 10.1063/5.0037246

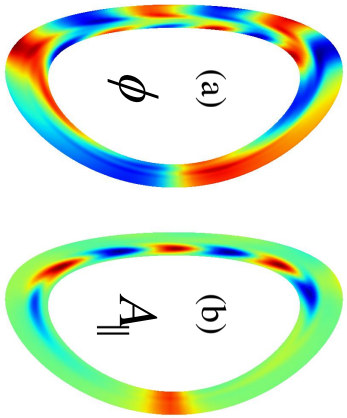

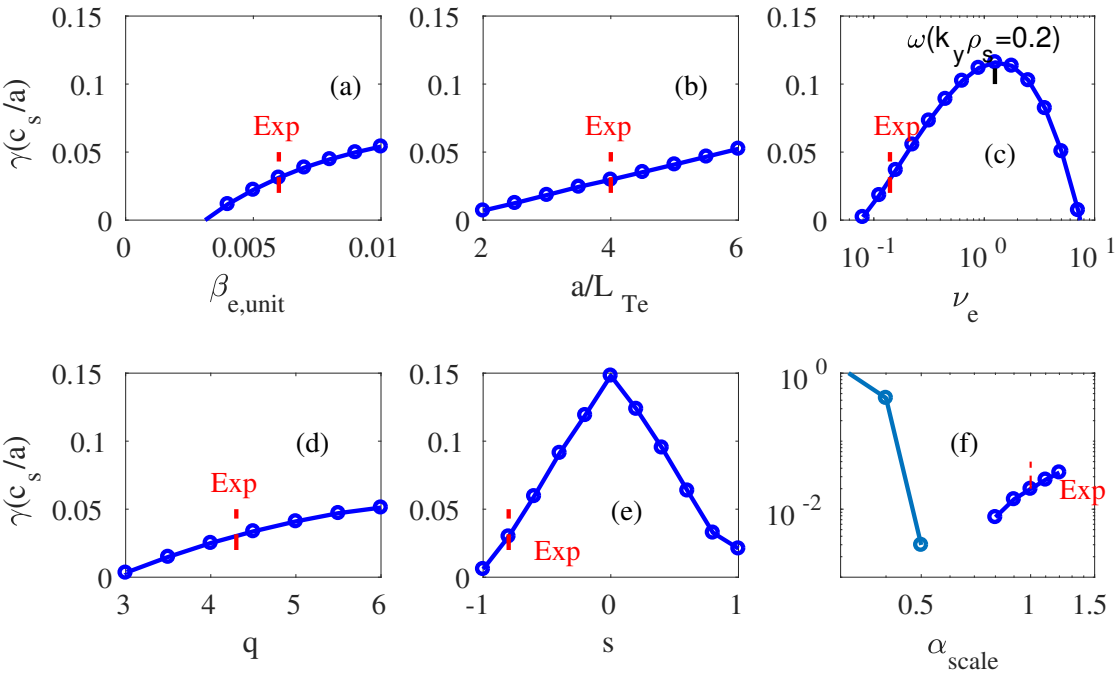

Physics of Plasmas

PLEASE CITE THIS ARTICLE AS DOI: 10.1063/5.0037246

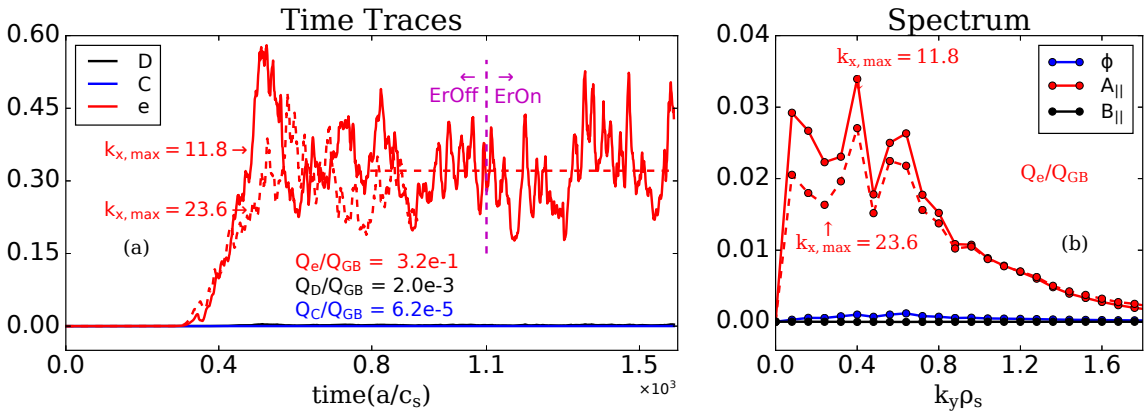

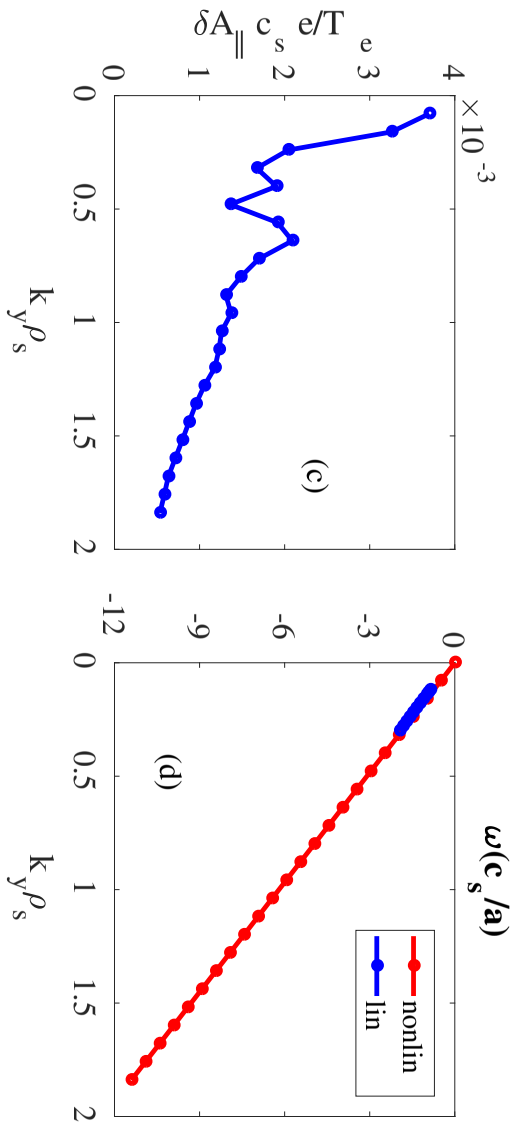

PLEASE CITE THIS ARTICLE AS DOI: 10.1063/5.0037246

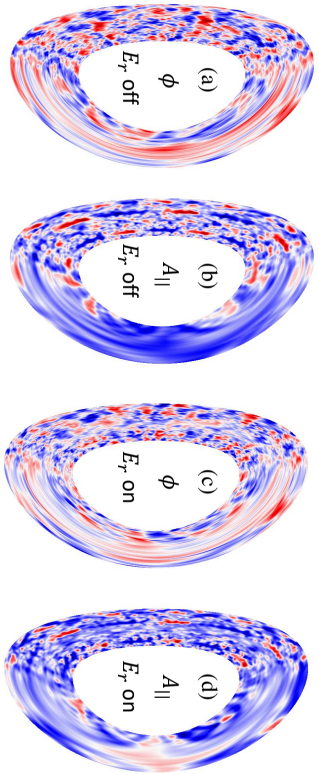

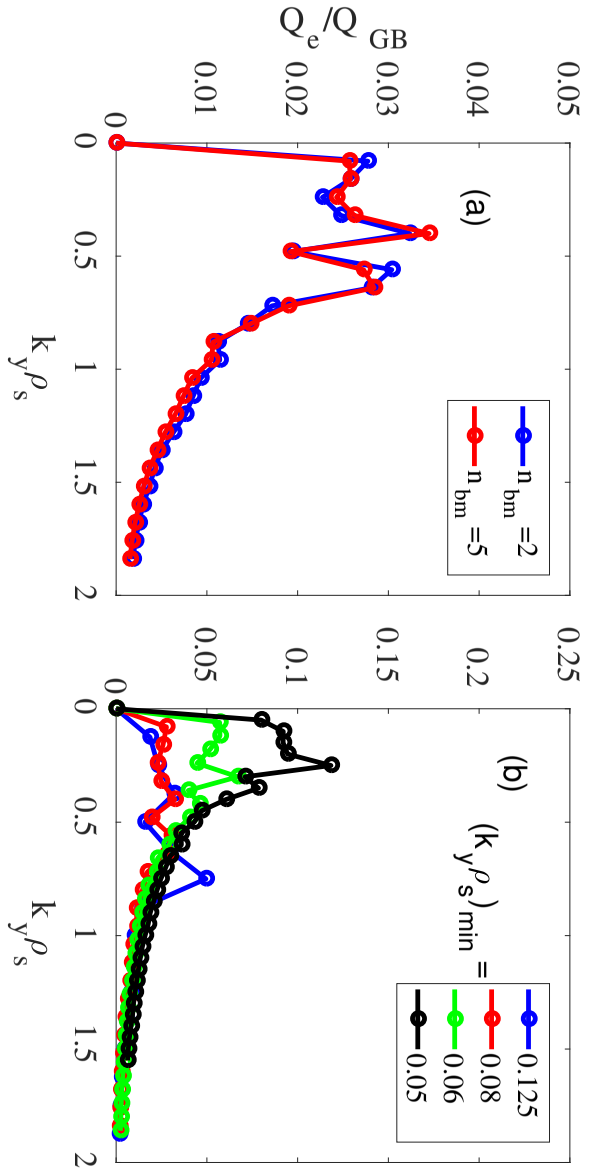

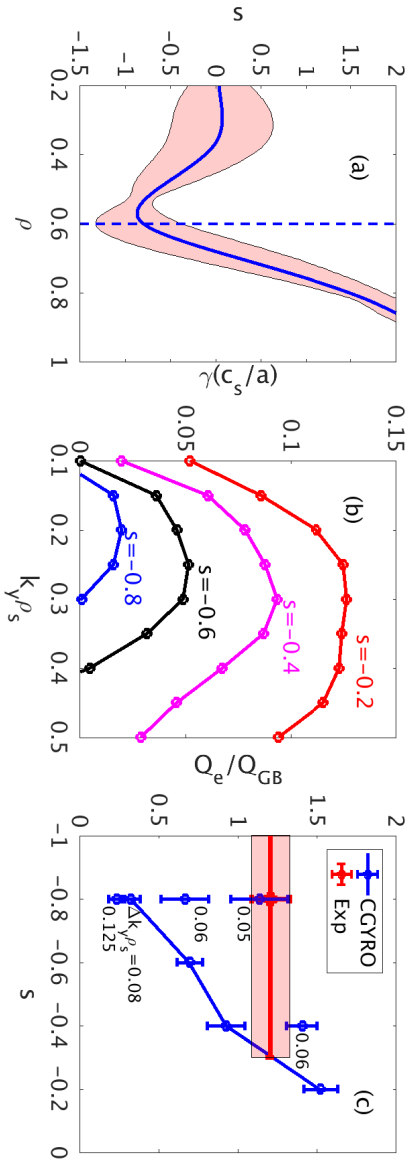

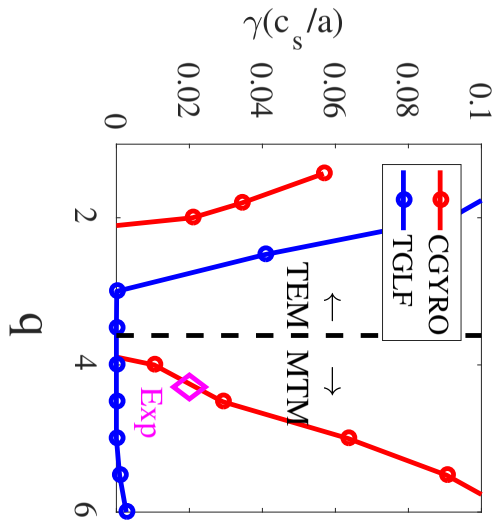

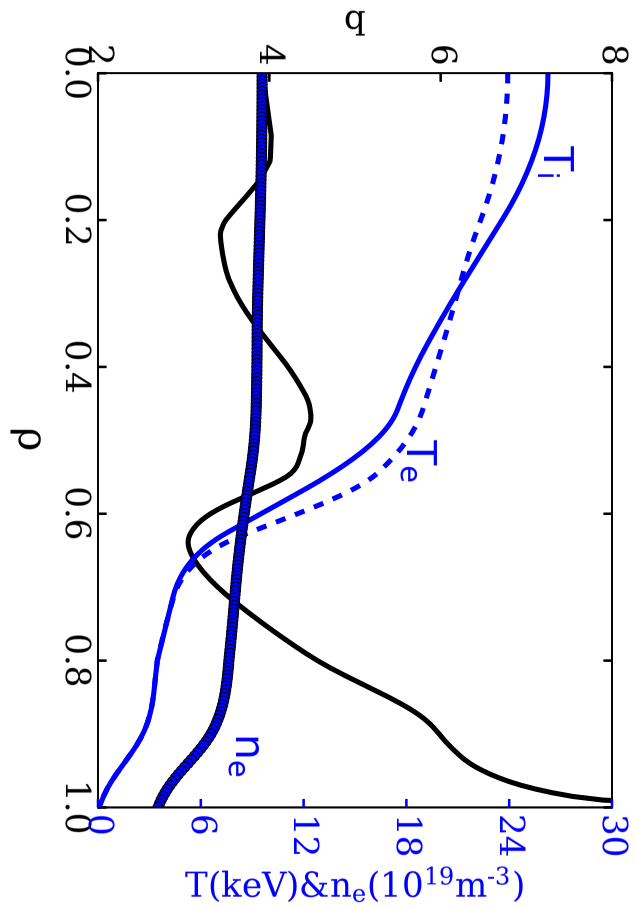

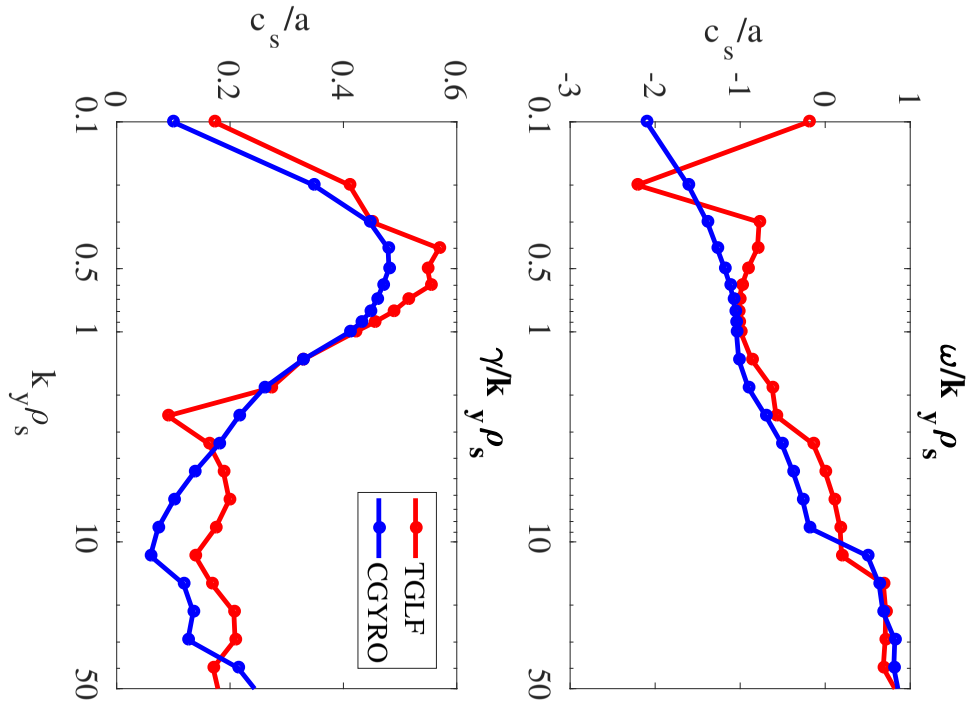

PLEASE CITE THIS ARTICLE AS DOI: 10.1063/5.0037246